

# Cross-correlation of cosmic voids with thermal Sunyaev-Zel'dovich data

Gang Li,<sup>1,2</sup> Yin-Zhe Ma<sup>3,4</sup>★ Denis Tramonte,<sup>5,1</sup> Guo-Liang Li<sup>1</sup>

<sup>1</sup>Purple Mountain Observatory, Chinese Academy of Sciences, Nanjing 210023, China

<sup>2</sup>School of Astronomy and Space Science, University of Science and Technology of China, Hefei 230026, China

<sup>3</sup>Department of Physics, Stellenbosch University, Matieland 7602, South Africa

<sup>4</sup>National Institute for Theoretical and Computational Sciences (NITheCS), Stellenbosch University, Matieland 7602, South Africa

<sup>5</sup>Department of Physics, Xi'an Jiaotong-Liverpool University, Suzhou 215123, China

Accepted XXX. Received YYY; in original form ZZZ

## ABSTRACT

We provide a measurement of the deficit in the Sunyaev-Zel'dovich Compton- $\gamma$  signal towards cosmic voids, by stacking a catalogue of 97,090 voids constructed with BOSS-DR12 data, on the  $y$  maps built on data from the Atacama Cosmology Telescope (ACT) DR4 and the *Planck* satellite. We detect the void signal with a significance of  $7.3\sigma$  with ACT and  $9.7\sigma$  with *Planck*, obtaining agreements in the associated void radial  $y$  profiles extracted from both maps. The inner-void profile (for angular separations within the void angular radius) is reconstructed with significances of  $4.7\sigma$  and  $6.1\sigma$  with ACT and *Planck*, respectively; we model such profile using a simple model that assumes uniform gas (under)density and temperature, which enables us to place constraints on the product  $(-\delta_v T_e)$  of the void density contrast (negative) and the electron temperature. The best-fit values from the two data sets are  $(-\delta_v T_e) = (6.5 \pm 2.3) \times 10^5$  K for ACT and  $(8.6 \pm 2.1) \times 10^5$  K for *Planck* (68% C.L.), which are in good agreement under uncertainty. The data allow us to place lower limits on the expected void electron temperature at  $2.7 \times 10^5$  K with ACT and  $5.1 \times 10^5$  K with *Planck* (95% C.L.); these results can transform into upper limits for the ratio between the void electron density and the cosmic mean as  $n_e^v/\bar{n}_e \leq 0.73$  and  $0.49$  (95% C.L.), respectively. Our findings prove the feasibility of using tSZ observations to constrain the gas properties inside cosmic voids, and confirm that voids are under-pressured regions compared to their surroundings.

**Key words:** large-scale structure of Universe – cosmology: observations

## 1 INTRODUCTION

Cosmic voids are the largest under-dense regions filling most of the volume in the Universe, and contain abundant cosmological information for probing dark energy, cosmic structure growth, and galaxy formation (Lavaux & Wandelt 2012; Pisani et al. 2015; Cai et al. 2015; Beygu et al. 2017; Falck et al. 2018; Pustilnik et al. 2019; Hamaus et al. 2020; Aubert et al. 2022; Ceccarelli et al. 2022). Nonetheless, in general, void properties have not been investigated sufficiently, as their low-density environment makes it challenging to find observational tracers. In recent years, there have been several studies aimed at cross-correlating voids with other large-scale structure (LSS) tracers. For example, voids have been detected by using different LSS gravitational lensing data (Melchior et al. 2014; Clampitt & Jain 2015; Sánchez et al. 2017; Fang et al. 2019), and CMB lensing maps (Cai et al. 2017; Raghunathan et al. 2020; Vielzeuf et al. 2021). However, because the lensing signal is only sensitive to the total matter density, cross-correlation with lensing data cannot dissect the baryonic gas from the underlying dark matter distribution.

Characterising gas inside voids is indeed a crucial problem in cosmology, as voids can possibly host the “missing baryons” in the galactic and super-galactic ecosystem (Haider et al. 2016; Martizzi

et al. 2019), which are particularly challenging to detect<sup>1</sup>. Recent observations from OVII absorption systems (Nicastrò et al. 2018) and fast radio burst (Macquart et al. 2020) showed that most of the undetected baryons are likely in form of a diffuse and ionised plasma, such as the cool phase of the inter-galactic medium (IGM,  $T < 10^5$  K) and the warm-hot intergalactic medium (WHIM,  $10^5 < T < 10^7$  K). However, because of the low-density ( $n_H < 10^{-4}(1+z)$  cm<sup>-3</sup>) of this diffuse gas, it is difficult to trace out the baryons location and pin down their detailed physical properties. Cosmological hydrodynamical simulations suggest that a significant portion of baryons is indeed contained within cosmic voids, in a multi-phase gas state (Haider et al. 2016; Martizzi et al. 2019). It is therefore necessary to carry out a detailed observational study of gas inside cosmic voids.

In this work, we use the thermal Sunyaev-Zel'dovich (tSZ) effect (Sunyaev & Zeldovich 1970) to probe the warm-hot gas that is possibly contained inside cosmic voids. The tSZ effect arises from the inverse Compton scattering of CMB photons by the warm-hot ionized electrons in the LSS. The amplitude of tSZ effect is captured by the Compton- $\gamma$  parameter, which is the integrated electron pressure along the line-of-sight (LoS):

$$y = \frac{\sigma_T}{m_e c^2} \int P_e dl, \quad (1)$$

<sup>1</sup> For a general description of the missing baryon problem, please refer to Fukugita & Peebles (2004); Bregman (2007) and Shull et al. (2012).

★ Corresponding author: Y.-Z. Ma, mayinzhe@sun.ac.za

where  $P_e \equiv k_B n_e T_e$  is the gas pressure ( $n_e$ ,  $T_e$  being the electron density and temperature and  $k_B$  being the Boltzmann constant),  $\sigma_T$  is the Thomson cross section,  $m_e$  is the electron mass, and  $c$  is the speed of light. In recent years, several works have been carried out to extract the WHIM's tSZ effect from cosmic filaments (Tanimura et al. 2019; de Graaff et al. 2019), intercluster gas (Planck Collaboration et al. 2013; Bonjean et al. 2018), and correlated gas in and between dark matter halos (Ma et al. 2015; Hojjati et al. 2015, 2017; Makiya et al. 2018; Ma et al. 2021; Ibitoye et al. 2022; Pandey et al. 2022; Tramonte et al. 2023). More importantly, Alonso et al. (2018) reported the first detection of tSZ signal towards cosmic voids at  $3.4\sigma$  confidence level (C.L.), by stacking SDSS CMASS voids<sup>2</sup> on the *Planck* Compton- $y$  map. The results indicate that voids are under-pressured relative to the cosmic mean. Such a detection corroborates the relevant abundance of warm-hot gas in voids and their surroundings. In order to further investigate the gas properties inside voids, we need to obtain more precise measurements of its density and temperature, and compare them with the theoretical modelling. This is the aim of this work.

In the following, we will investigate the gas inside voids by using Compton- $y$  maps from both the *Planck* 2015 data release and the Atacama Cosmology Telescope (ACT) Data Release 4 (DR4), where the latter has a higher angular resolution than the former. In addition, we will use a void catalogue constructed with a novel parameter-free cosmological void finder (Zhao et al. 2016), which renders in total 97,090 voids over the ACT footprint; this sample is  $\sim 125$  times the size of the CMASS-based void sample used in Alonso et al. (2018). Besides stacking these voids on the  $y$  maps, we will build a gas density and temperature model to interpret the measurement of the reconstructed mean void Compton- $y$  profile.

The rest of the paper is organized as follows. Sec. 2 describes the Compton- $y$  maps and void data we use. Sec. 3 presents the stacking method, results and the inclusion of possible CIB contaminations; we then build a theoretical model to quantify the void gas characteristics in Sec. 4. We summarise our findings and discuss their physical implications in Sec. 5. Throughout this work, we adopt a spatially-flat  $\Lambda$ CDM cosmology with the relevant parameters fixed to the values  $h = 0.68$  and  $\Omega_b h^2 = 0.0224$  (Planck Collaboration et al. 2020).

## 2 DATA

### 2.1 Compton- $y$ maps

We use the Compton- $y$  maps obtained from ACT DR4 data that is presented in Madhavacheril et al. (2020). The ACT Compton- $y$  maps are the first wide-area ( $\sim 2,100 \text{ deg}^2$ ), arc-minute resolution component separated maps of the tSZ effect. They are constructed by implementing a component separation method based on the Internal Linear Combination (ILC) approach (Remazeilles et al. 2011), combining *Planck* individual frequency maps from 30 to 545 GHz and ACT data at 98 and 150 GHz. The ACT Compton- $y$  maps have an unprecedented high resolution of FWHM = 1.6 arc-minutes, and cover two separated regions, namely the D56 region ( $\sim 456 \text{ deg}^2$ ), and the larger BN region ( $\sim 1,633 \text{ deg}^2$ ).

A number of potential foreground contaminants such as the Galactic plane or radio sources may affect the cross-correlation analysis between the tSZ maps and other LSS tracers (Madhavacheril et al.

2020). While the ILC pipeline generally does not fully eliminate the foreground residuals, there is also no specific mask released by the ACT collaboration that is tailored to tSZ analyses; hence, we adopt the *Planck* 40% Galactic plane mask combined with the *Planck* point-source mask (Planck Collaboration et al. 2016c), and project it on the ACT footprint (upper panels in Fig. 1).

Apart from the ACT  $y$ -maps, another available full-sky Compton- $y$  map was provided as part of *Planck* 2015 data release (Planck Collaboration et al. 2016a). The *Planck*  $y$ -map is pixelized on a 2D spherical surface in HEALPix format with resolution  $N_{\text{side}} = 2048$  (Górski et al. 2005). There are two versions of the *Planck*  $y$ -map, based on different reconstruction methods: the Modified Internal Linear Combination Algorithm (MILCA, Hurier et al. 2013) and the Needlet Internal Linear Combination (NILC, Remazeilles et al. 2011); both are derived from multi-band combinations of *Planck* intensity maps from 30 to 857 GHz. The NILC  $y$ -map has higher noise on large scales compared to the MILCA  $y$ -map, although it has been found that the former basically gives results consistent with the latter even for large-scale studies (Vikram et al. 2017; Alonso et al. 2018; Tanimura et al. 2019). Nonetheless, since voids usually subtend large angular scales, to avoid potential noise contaminations, we will only employ the MILCA  $y$ -map for our void stacking analysis.

The *Planck*  $y$ -map has an angular resolution of FWHM = 10 arc-minutes, lower than the ACT  $y$ -map. In order to allow a better comparison with the ACT  $y$ -map results, we first project the *Planck*  $y$ -map on the ACT footprint regions using the `pixell` package<sup>3</sup>, which also ensures the same stacking pipeline can be used for both versions of the Compton- $y$  map. The same mask is also used for both *Planck* and ACT  $y$ -maps.

The final masked ACT and *Planck*  $y$  maps that we are going to employ in this study are shown in the top and bottom panels of Fig. 1<sup>4</sup>.

### 2.2 Void catalogue

We use the void catalogue constructed by Zhao et al. (2016), who employed a novel parameter-free cosmological void finder (DIVE, Delaunay Triangulation Void findER) based on a Delaunay Triangulation (DT) algorithm. The DIVE algorithm can efficiently compute the empty spheres constrained by a discrete set of tracers; hereafter we shall label the resulting voids as *DT voids*. The DT void catalogue is constructed from the BOSS-DR12 galaxy data, which include both CMASS (a subsample of BOSS galaxies with redshift  $z > 0.45$ ) and LOWZ (a subsample of BOSS galaxies with redshift  $z < 0.45$ ) galaxies (Alam et al. 2017; Tanidis & Camera 2021). The DT voids span the redshift range  $0.1 < z < 0.8$ , and the (comoving) radius range  $1.0h^{-1}\text{Mpc} < R_v < 99.3h^{-1}\text{Mpc}$ ; the full DT void catalogue contains in total 7,886,816 voids, of which 5,713,918 in the northern sky and 2,172,898 in the southern sky.

In our analysis we will only consider voids with redshift in the range  $0.2 < z < 0.4$  and radius in the comoving range  $15.0h^{-1}\text{Mpc} < R_v < 25.0h^{-1}\text{Mpc}$ ; such a selection can indeed ensure a sufficient statistics for the stacking analysis, while avoiding uncertainties in the reconstructed void properties deriving from the boundaries of the catalogue. We then select the voids that are completely overlapping with the ACT  $y$ -map footprint, ensuring that the separation between their centres and the map boundaries is not smaller than two times

<sup>2</sup> Alonso et al. (2018) void catalogue is constructed from the SDSS-DR12 CMASS galaxy sample, and can be downloaded at <http://lss.phy.vanderbilt.edu/voids/>.

<sup>3</sup> <https://pixell.readthedocs.io/en/latest/>

<sup>4</sup> ACT footprint with the projected masks is also shown in Fig. 1 of Tramonte et al. (2023).

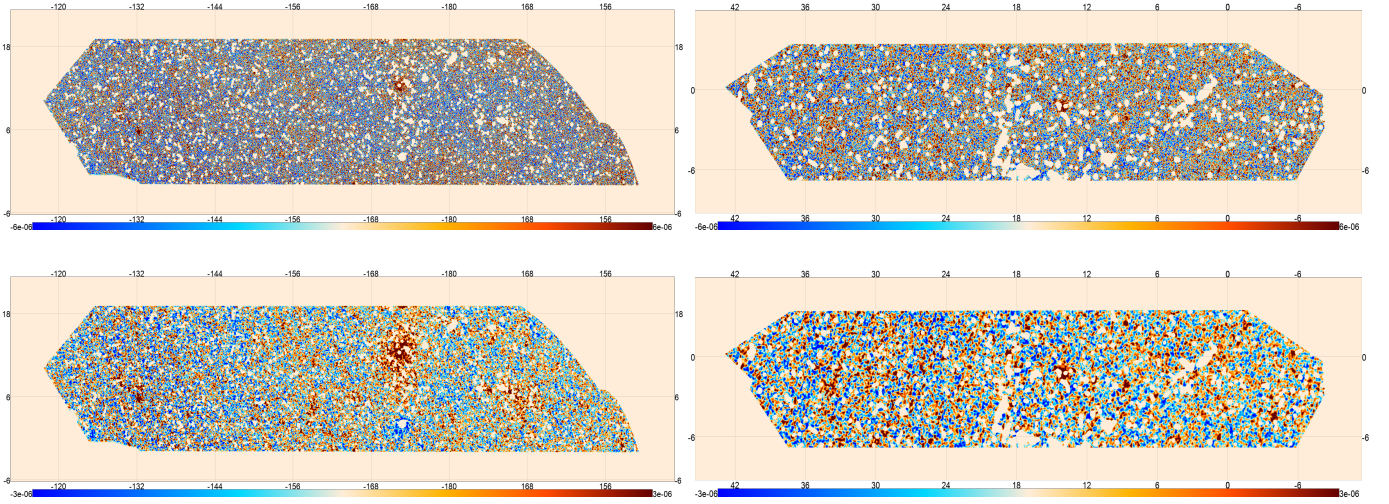


**Figure 1.** Combined Compton- $y$  maps with the projected *Planck* Galactic Plane and point sources masks. The *left* column is the ACT BN-region, and the *right* is ACT D56 region. The *upper* row shows the actual ACT data and the *lower* row shows the *Planck* data on ACT region. The vertical axis (declination) and horizontal axis (right ascension) are labeled in degrees.

their projected angular radius. After these steps, there are 81,053 and 16,037 voids left in BN and D56 regions, respectively. The mean redshift and effective (comoving) radius of the 97,090 selected voids are  $z = 0.32$  and  $18 h^{-1}\text{Mpc}$ , which corresponds to the effective physical radius  $R_{\text{eff}} = 13.6 h^{-1}\text{Mpc}$ .

Zhao et al. (2016) also generated  $1.4 \times 10^8$  mock voids ( $4 \times 10^7$  voids in the southern sky,  $10^8$  voids in the northern sky), which we shall employ for the statistical characterisation of our results. Again, we first select the mock voids that satisfy the redshift and radius conditions detailed above, which leaves 9,928,676 mock voids in total. The subsequent positional query leaves 1,522,072 mock voids over the BN region and 317,829 mock voids over the D56 region. Finally, we construct 1000 different mock catalogues for each region, by randomly choosing each time 81,053 and 16,037 mock voids out of these BN and D56 mock samples, respectively. The mock catalogues are used to deduct the background signal as well as to compute the covariance matrix and the significance of our measurements, as detailed in Sec. 3.

### 3 MEASUREMENTS

#### 3.1 Stacking analysis

To extract the tSZ signal around voids, we stack the Compton- $y$  map at the position of the selected voids. The  $y$ -maps are pixelized on a 2D flat plane and we use the `pixell` Python package<sup>5</sup> to extract all pixels within a square area centred on each void and with side equal to four times the void angular radius,  $4\theta_v$ , where  $\theta_v \equiv R_{\text{eff}}/D_A$ , with  $D_A$  the angular diameter distance to the void. We then scale the angular separation of each pixel from the void central pixel by the void effective radius ( $\theta/\theta_v$ ); this operations ensures that, prior to the stack, all voids are brought to a uniform size. The scaled pixels are then binned into the same grid coordinate system of  $-2 < \Delta\text{RA}/\theta_v < +2$  and  $-2 < \Delta\text{Dec}/\theta_v < +2$ , divided into  $40 \times 40$  bins. For the generic  $i$ -th void, this procedure is repeated for both the Compton- $y$  map, yielding a void signal map  $y_i$ , and for the mask, yielding a void weight map  $W_i$  (the latter only has possible values 0 and 1). For the

full void sample, the resulting stacked signal map is then obtained as the weighted average:

$$y_{\text{stack}} = \frac{1}{W_{\text{stack}}} \sum_{i=1}^{N_v} y_i W_i, \quad (2)$$

where  $N_v$  is the number of stacked voids, and

$$W_{\text{stack}} = \sum_{i=1}^{N_v} W_i \quad (3)$$

is the total weight for this stack.

We obtain this way two different stack maps, one for each of the two ACT patches. The final, combined map can be obtained with a further weighted average as:

$$y_{\text{tot}} = \left[ \sum_{i=1}^{N_{\text{BN}}} y_i^{\text{BN}} W_i^{\text{BN}} + \sum_{i=1}^{N_{\text{D56}}} y_i^{\text{D56}} W_i^{\text{D56}} \right] / \left[ W_{\text{stack}}^{\text{BN}} + W_{\text{stack}}^{\text{D56}} \right]. \quad (4)$$

The procedure described above is also repeated for each of the mock catalogues, thus yielding 1,000 mock  $y$ -stack maps; we label  $y^{(k)}$  the stacked signal map for the  $k$ -th mock catalogue. These mock stacks are representative of the background contribution to the signal, which includes additional effects such as incomplete sky coverage, large-scale monopole contribution and residual systematics. Indeed, because we are stacking both the real void catalogue and the mock catalogues on the same map, any of such systematic effects affecting the latter will be captured by both the catalogue stack and the mock stacks. Our final reconstruction of the void signal is then obtained by subtracting from the real void stack, the average of the mock stack, which we can consider as a ‘‘background’’ term calculated as:

$$\bar{y} = y_{\text{tot}} - \frac{1}{N_m} \sum_{k=1}^{N_m} y^{(k)}, \quad (5)$$

where  $N_m = 1000$  is the number of mock samples. We suppress the overhead bar in  $\bar{y}$  for abbreviation in the following. A similar approach was also adopted in Alonso et al. (2018).

In Figure 2 we show the 2-dimensional stack maps, while the corresponding 1-dimensional radial profiles are plotted in Fig. 3. Because the 2-D map are pixelised in  $40 \times 40$  grids, we use 20

<sup>5</sup> <https://pixell.readthedocs.io/en/latest/>

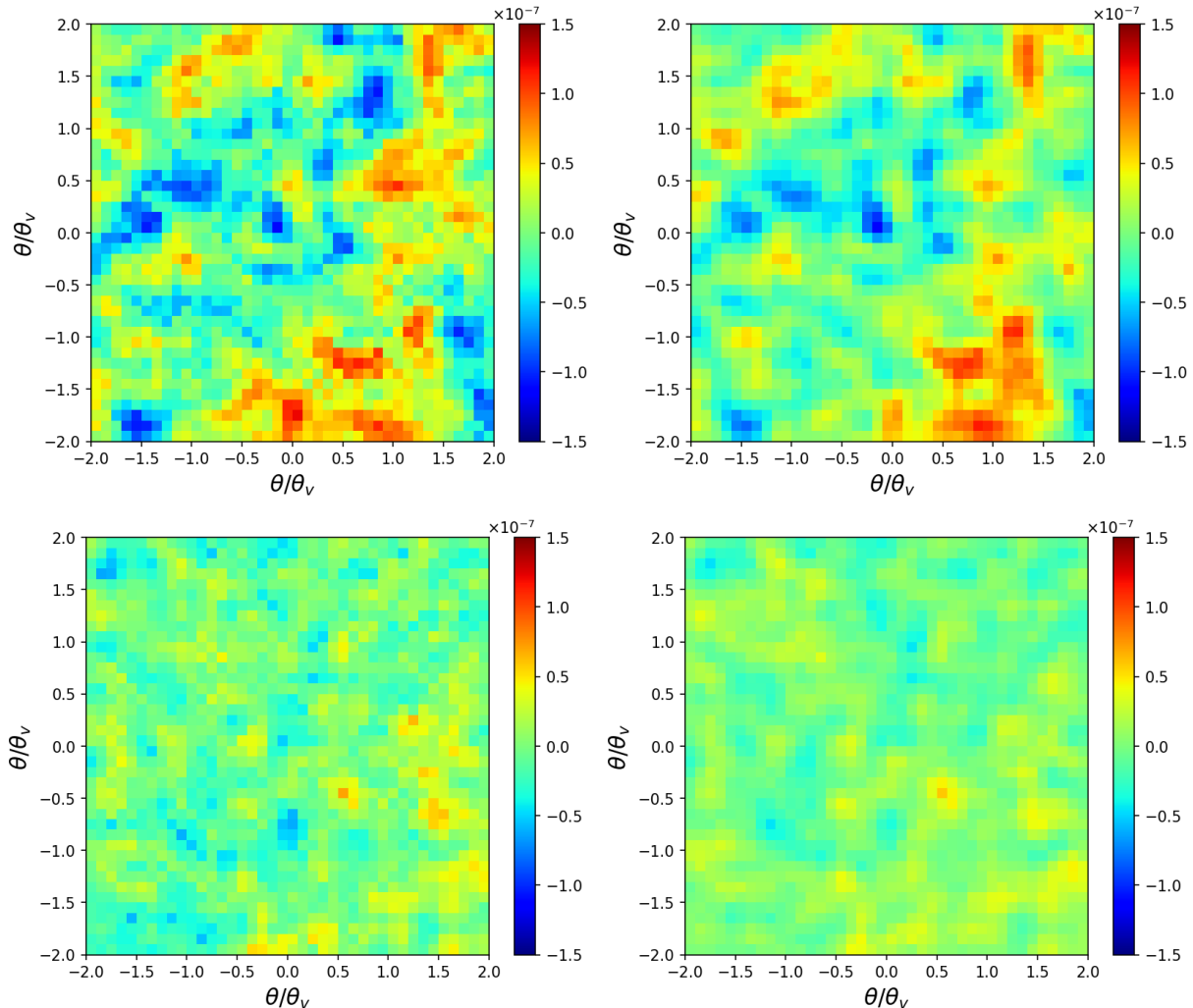


**Figure 2.** *Top:* the 2D signal maps obtained by stacking the DT void sample on ACT (*left*) and *Planck* (*right*) Compton- $y$  maps. *Bottom:* same as in the top row, but showing this time the results obtained using a random (mock) void catalogue.

racial bins to compute the average  $y$  value within each annulus of the 2-D map. A signal amplitude deficit can be seen in the region  $\theta/\theta_v < 1$  both in the stacked 2D maps and also (more clearly) in the 1D profile. For comparison, Figure 2 also shows the stack maps obtained with one of the mock void catalogues: we can see that there is no central deficit when stacking the random catalogues (stacks for other mocks are qualitatively similar to the one shown here), which supports the interpretation of the central amplitude decrease, when stacking the real catalogue, as void signal. One can also appreciate similar patterns in both the 2D ACT and *Planck* stack maps using real voids, as well as similar trends in the associated 1D profiles. Figure 3 shows the larger errors near the center of the stacked voids than outer radii. This comes from the fact that there are larger fluctuations in the center of the voids (the negative peak amplitude) compared to the outskirts where an average of zero level is more consistent from void to void. As a result, the smaller fluctuations in the outskirts and higher fluctuations in the center produce variances of the errors in different radii.

Finally, we notice that the void profile amplitude approaches zero at the unit scaled void radius ( $\theta/\theta_v \simeq 1$ ), while outside the void area we can observe some signal fluctuations that can be ascribed to the gas in the surrounding large-scale structures. We remind that

for each void we trim a local square  $y$ -map with the side equal to four times the void angular radius, in such a way as to contain the circular region of  $2 \times \theta_v$  centred on the void; this is also the outer edge to which we reconstruct the void profile. There is no standard recipe for the optimal outer radius in this kind of study; clearly it is possible to choose an arbitrarily large radius (e.g.  $\geq 3 \times \theta_v$ ) to explore the signal behaviour outside the void radius. This, however, would come at the price of lowering the statistics of our sample, as only the voids that are fully overlapping with the ACT footprint over their full local (trimmed) square map are considered in the stack: extending the outer edge from  $2 \times \theta_v$  to  $3 \times \theta_v$  will imply less voids can make this selection, leading to a lower S/N ratio in the final profile reconstruction. Besides, in this analysis we are mostly interested in the properties of the gas in the void inner region, and in principles, the void radius should mark the boundary of each void, as the former is associated with the corresponding circumspheres defined in the DIVE algorithm (Zhao et al. 2016). For these reasons, in our analysis we choose  $4\theta_v$  as the side of the square stack map, i.e.  $2 \times \theta_v$  as the radius of the circular region (we have also verified that beyond  $2\theta_v$  the signal amplitude drops back down to zero).

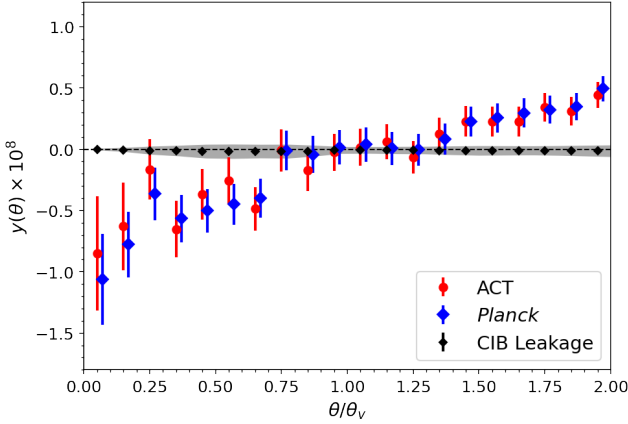


**Figure 3.** Reconstructed mean radial Compton- $y$  profile for the DT voids measured on ACT (red circles) and *Planck* (blue squares) stacked maps (top row of Fig. 2). The black diamonds show the best-fit CIB leakage in the stacked void profile, by scaling the stacked void signal on the *Planck* 545 GHz temperature map with the  $\alpha_{\text{CIB}}$  parameter. The grey band around the zero line shows the range of CIB leakage by allowing  $\pm 1\sigma$  uncertainty on  $\alpha_{\text{CIB}}$ . The estimation of  $\alpha_{\text{CIB}}$  is described in Sec. 3.3. The total significance of the detection is  $7.3\sigma$  for ACT and  $9.7\sigma$  for *Planck*, while the inner profile (considering only the points for which  $\theta/\theta_v \leq 1$ ) is detected at  $4.7\sigma$  with ACT and  $6.1\sigma$  with *Planck*.

### 3.2 Statistical characterisation

We estimate the covariance matrix  $C_{ij}$  for the reconstructed  $y$  profile employing the 1000 measured  $y$  profiles obtained with the mock catalogues:

$$C_{ij} = \frac{1}{N_m} \sum_{k=1}^{N_m} (y_i^{(k)} - \langle y_i \rangle) (y_j^{(k)} - \langle y_j \rangle) \quad (6)$$

where  $i, j$  index individual angular bins,  $y_i^{(k)}$  is the measurement from the  $k$ -th mock, and  $\langle y_i \rangle$  is the average across mocks. The correlation matrix, defined as

$$R_{ij} = \frac{C_{ij}}{\sqrt{C_{ii}C_{jj}}}, \quad (7)$$

quantifies the level of correlation for off-diagonal bin pairs, and is plotted in Fig. 4. We notice that the correlation matrices contain significant non-zero off-diagonal elements, which is likely a result of the beam smoothing in the Compton  $y$ -maps and also the mixing of scales occurring when rescaling the size of individual void maps before stacking. The uncertainties on the measured  $y$  profiles can be quantified by the diagonal elements of the covariance matrix, yielding comparable error bars between ACT and *Planck* cases.

To estimate the significance of our measurements, we compute the  $\chi^2$  with a null hypothesis. In general, the total  $\chi^2$  can be calculated as:

$$\chi^2 = \sum_{i,j} (y_i - y_i^{\text{mod}}) I_{ij} (y_j - y_j^{\text{mod}}), \quad (8)$$

where  $y_i$  is the measured Compton profile and  $y_i^{\text{mod}}$  is instead the given model; for the null hypothesis,  $y^{\text{mod}} = 0$ . The quantity  $I_{ij}$  is the inverse covariance matrix, bias-corrected by included an extra factor as (Hartlap et al. 2007):

$$I_{ij} = \frac{N_m - N_b - 2}{N_m - 1} (C^{-1})_{ij}, \quad (9)$$

where  $N_b = 20$  is the number of radial bins. We can also apply Eq. (8) to each mock profiles, which yields 1000  $\chi^2$  values for the null hypothesis; the distribution of these values, for both ACT and *Planck*, is plotted in Fig. 5. This distribution should be described by a chi-squared distribution with 20 degrees of freedom, which is computed analytically and overplotted to Fig. 5. We find indeed a good match between the theoretical curve and the distributions obtained from the mock  $\chi^2$  values.

For the case of the real data stack, the  $\chi^2$  for the null hypothesis ( $y^{\text{mod}} = 0$ ) is evaluated at  $\chi^2_{\text{ACT}} = 53.67$  for ACT and  $\chi^2_{\text{Planck}} = 93.91$  for *Planck*, for the number of degree of freedom (dof) equal to  $N_b = 20$ . These correspond to the detection significance of  $7.3\sigma$  for ACT and  $9.7\sigma$  for *Planck* measurements against the null signal.

We notice that, as far as the detection significance is concerned, there is no advantage in using ACT  $y$ -map over using *Planck*  $y$ -map, despite ACT considerably higher resolution. This could be ascribed primarily to the fact that voids are extended objects with mean radial angular sizes of  $\theta_v \approx 1.2$  deg, implying that their signature is well resolved already with the resolution available in the *Planck* map. In addition, we notice that, in fact, the smoothing effect caused by the larger *Planck* beam typically determines lower background fluctuations in the random stacks, as it is visible in Fig. 2, which results in *Planck* error bars being slightly smaller than the ones obtained for ACT, as one can see from Fig. 3; this effect contributes to the slight higher value of *Planck* significance when compared to ACT results.

It is worth mentioning, however, that Alonso et al. (2018) only adopted a subsample of voids selected based on their high-significance identification by the void-finder algorithm, with the purpose of increasing the signal-to-noise (S/N) ratio of their measurements. For this reason, it is not meaningful to infer the expected S/N ratio with our sample purely based on the sample size. Another (this time technical) difference from the analysis in Alonso et al. (2018) is that, while they perform a void stack on spherical coordinates (*Planck*  $y$ -map), we will perform it on a 2-D plane  $y$ -map (ACT). For a consistency check, we have verified that the stack of the same void sample used in Alonso et al. (2018), this time on the plane-projected *Planck* map and using our stacking pipeline, provide results consistent with the ones presented by the authors.

### 3.3 CIB contamination

One of the main sources of systematic uncertainties comes from the cosmic infrared background (CIB; Planck Collaboration et al. 2016b), that can contaminate the reconstructed tSZ  $y$ -maps. Following previous studies (Vikram et al. 2017; Hill & Spergel 2014; Alonso et al. 2018), we use *Planck* 545 GHz temperature map (in units MJy  $\text{sr}^{-1}$ ) as the proxy for CIB contamination, to quantify its potential influence on our tSZ measurement. The measured Compton signal from our stacks,  $y_{\text{obs}}$  can thus be modelled as a combination of the true, uncontaminated signal  $y_{\text{true}}$ , and the CIB contribution, as:

$$y_{\text{obs}} = y_{\text{true}} + \alpha_{\text{CIB}} T_{545}, \quad (10)$$

where  $T_{545}$  is the 545 GHz intensity map tracing the CIB, and  $\alpha_{\text{CIB}}$  is a scalar parameter gauging the CIB contribution. Here we take the fiducial value  $\alpha_{\text{CIB}} = (2.3 \pm 6.6) \times 10^{-7}$  MJy $^{-1}$  sr, which was derived from the auto-correlation of the 545 GHz map and its cross-correlation with the *Planck*  $y$  map in Alonso et al. (2018).

In order to quantify the CIB contribution to our measured profiles, we can adopt the strategy in Alonso et al. (2018) and stack the same set of voids on the  $T_{545}$  map, to extract a mean  $T_{545}$  void profile. The result is plotted in Fig. 6, where the lower amplitude at small separations can be interpreted as the cross-correlation signal between

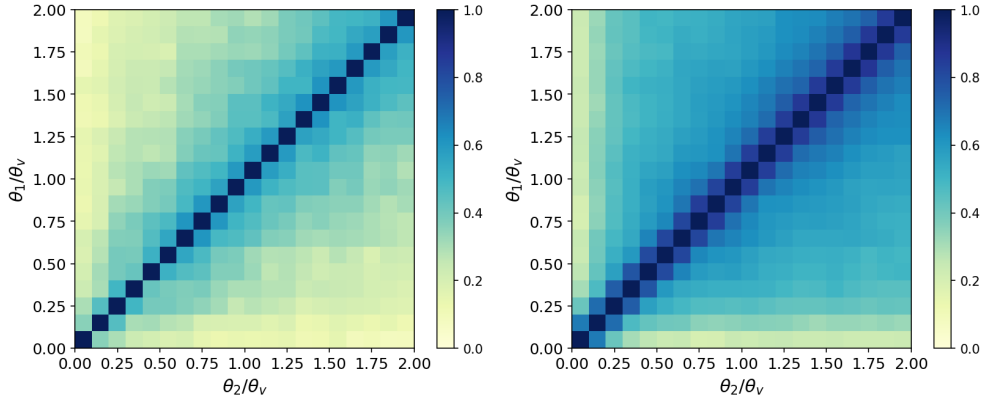


**Figure 4.** The correlation matrices (Eq. (7)) for the measured radial tSZ profile around voids, for both the case of ACT (*left*) and *Planck* (*right*) y maps. These correlation matrices are estimated from the stack results of 1,000 mock void catalogues.

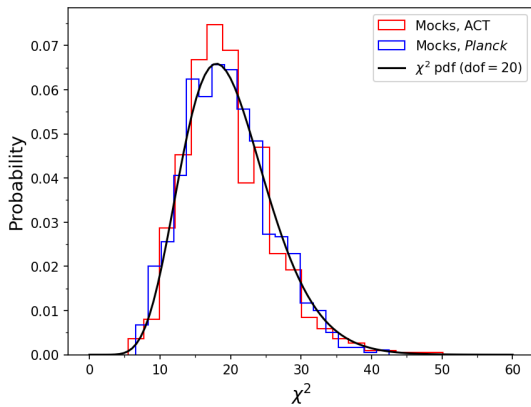


**Figure 5.** The probability distribution of  $\chi^2$  values for the 1,000 mock void catalogues, plotted as a histogram for both ACT and *Planck* results. Because the mock voids and the y maps are uncorrelated, this distribution is very close to a “chi-squared” distribution with 20 degrees of freedom, which is also overlotted as the solid black line.

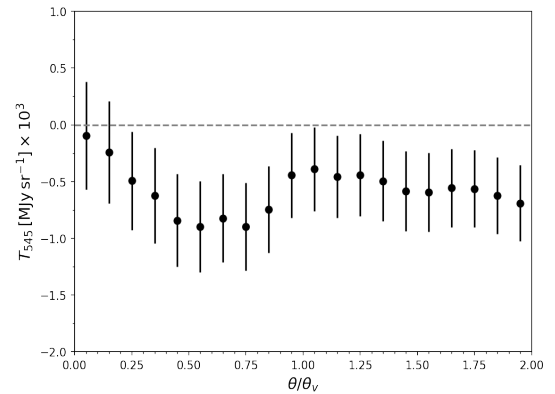


**Figure 6.** The stacked void profile on *Planck* 545 GHz temperature map, which can be regarded as a proxy for CIB contamination to our y measurement, when scaled by the  $\alpha_{\text{CIB}}$  factor (see also Fig. 3).

voids and the  $T_{545}$  map. This profile is then scaled by  $\alpha_{\text{CIB}}$  following Eq. (10).

The signal leakage due to CIB (that is  $\alpha_{\text{CIB}}T_{545}$ ) into the reconstructed y profiles is shown with black diamonds in Fig. 2, where we can see it is compatible with zero. The gray shaded region in Fig. 2 represents the  $1\text{-}\sigma$  uncertainty level of this leakage, which is computed by finding the maximum and minimum values of  $\alpha_{\text{CIB}} \times T_{545}(\theta)$  profile. One can see that this  $\pm 1\sigma$  variation band is also much smaller than the measured tSZ signal, so the CIB residual in our void stacks is practically negligible. We further verified this conclusion by employing the 545 GHz CIB map from (Planck Collaboration et al. 2016b), which separates the Galactic thermal dust emission from CIB anisotropies. The stack signal on this CIB map is also very small compared to the tSZ signal. Therefore, we conclude that the CIB contamination can be safely ignored in our stacking.

Finally, we comment on the effect of the telescope beam, which is convolved with the sky signal and may determine an amplitude dilution. However, we remind that the mean angular size of our voids is  $\sim 1.21$  deg, which is considerably more extended than the beam FWHM, even in the case of *Planck*. Hence, possible systematic effects introduced by the instrumental beam are negligible in our analysis.

#### 4 INFERENCE ON GAS PROPERTIES

In this section, we detail the theoretical model we adopt to describe our measured Compton void signal; specifically, we shall employ an isothermal model which assumes a uniform density of gas inside the void. The electron density  $n_e(\mathbf{x}, z)$  at any position  $\mathbf{x}$  in space at redshift  $z$  is related to the mean electron density  $\bar{n}_e$  at the same redshift via:

$$n_e(\mathbf{x}, z) = \bar{n}_e(z)(1 + \delta(\mathbf{x})), \quad (11)$$

where  $\delta(\mathbf{x})$  is the density contrast, and

$$\bar{n}_e(z) = \frac{\rho_b(z)}{\mu_e m_p} \quad (12)$$

is the cosmic mean electron density at redshift  $z$  (Ma & Zhao 2014). In this relation  $\mu_e \simeq 1.14$  is the mean mass per proton,  $m_p$  is the proton mass, and  $\rho_b(z) = \rho_{\text{cr}}\Omega_b(1+z)^3$  is the baryon density at redshift  $z$ , where  $\rho_{\text{cr}} = 1.879h^2 \times 10^{-29} \text{ g cm}^{-3}$  is the critical density of the Universe at present time, and  $\Omega_b$  is the baryon density parameter. In our modeling, we make the further simplifying assumption that the density contrast within the void is a constant, i.e.  $\delta(\mathbf{x}) \equiv \delta_v$ , which is expected to be negative.

We now calculate the measured Compton-y profile of a void with a uniform electron temperature and density profile given by Eq. (11). Because in the stacking process we subtract the background term

computed from random mock catalogues (Eq. (5)), the mean background  $y$ -value is effectively removed in the final observed  $y(\theta)$  profiles plotted in Fig. 3. We then subtract the same term in our theoretical modelling, effectively computing the contrast in the  $y$  signal between voids and the mean background, as:

$$\begin{aligned} y(r_\perp) &= \frac{\sigma_{\text{T}} k_{\text{B}}}{m_e c^2} \int [n_e(\mathbf{x}, z) - \bar{n}_e(z)] T_e dl \\ &= \frac{\sigma_{\text{T}} k_{\text{B}} \bar{n}_e(z) T_e \delta_v}{m_e c^2} \int_{r_\perp}^{R_{\text{eff}}} \frac{2r dr}{\sqrt{r^2 - r_\perp^2}} \\ &= \frac{2\sigma_{\text{T}} k_{\text{B}} \bar{n}_e(z) T_e \delta_v}{m_e c^2} \sqrt{R_{\text{eff}}^2 - r_\perp^2}, \end{aligned} \quad (13)$$

where  $r_\perp$  is the projected distance from the void centre to the LoS, and  $R_{\text{eff}}$  is the void effective (physical) radius. In Eq. (13), in the second equality, we changed the integration variable from the LoS distance  $l$  to the void radial separation  $r$ , the two being related by  $l \equiv \sqrt{r^2 - r_\perp^2}$ . We now substitute Eqs. (11) and (12) into Eq. (13) and write the expression as a function of the angular separation  $\theta$  from the void centre ( $\theta = r_\perp / D_A(z)$ ,  $D_A(z)$  being the angular diameter distance to the void effective redshift), which yields:

$$\begin{aligned} y(\theta/\theta_v) &= \frac{2\sigma_{\text{T}} k_{\text{B}} T_e R_v \delta_v}{m_e c^2} \left( \frac{\Omega_b \rho_{\text{cr}} (1+z)^3}{\mu_e m_p} \right) \sqrt{1 - \left( \frac{\theta}{\theta_v} \right)^2} \\ &= (7.1 \times 10^{-10}) \delta_v \left( \frac{T_e}{10^5 \text{ K}} \right) \sqrt{1 - \left( \frac{\theta}{\theta_v} \right)^2}, \end{aligned} \quad (14)$$

where  $\theta_v = R_{\text{eff}} / D_A(z)$ , and in the last equality we have substituted the values for the void effective radius and redshift in our sample.

The analytical  $y$  profile predicted by Eq. (14), as a function of the scaled angular separation from the void centre  $\theta/\theta_v$ , can be directly compared to our measured stacked profiles. As we do not know *a priori* the values for the electron temperature and the density contrast inside the voids, we can leave the product  $T_e \delta_v$  as a free parameter, and estimate its best-fit value against our data<sup>6</sup>. We sample the  $(-\delta_v)(T_e/10^5 \text{ K})$  over the range of  $[-2, 18]$  for 1,000 points, and calculate the likelihood from the  $\chi^2$  in Eq. (8); since we are only fitting for the void decrement signal, in order to not be biased by the neighboring structures we only limit the comparison between the data and the model prediction to the first 10 data points (up to the void radius). The resulting posterior distribution on the parameter, for both the fits on ACT and *Planck* data, is plotted in the left panel of Fig. 7, whereas the right panel shows the comparison between the corresponding predictions and the measurements for the  $y$  profiles. From the posterior distribution we can extract the following best-fit estimates for the parameter  $\delta_v T_e$ :

$$\delta T \equiv \left( -\delta_v \frac{T_e}{10^5 \text{ K}} \right) = \begin{cases} 6.5 \pm 2.3 (1\sigma) \pm 3.8 (2\sigma) & \text{ACT} \\ 8.6 \pm 2.1 (1\sigma) \pm 3.5 (2\sigma) & \text{Planck}, \end{cases} \quad (15)$$

where the negative sign accounts for the fact that we are fitting a decrement in the  $y$  amplitude inside the void with respect to the mean background value. As for the goodness of this fit, it can be quantified by the  $\chi^2$  computed using Eq. (8), where this time  $y^{\text{mod}}$  is the predicted profile computed using Eq. (14) and each of the best-fit values from Eq. (15). It is actually more meaningful to quote the reduced chi-squared  $\chi_r^2$ , computed as the ratio between the chi-squared from Eq. (8) and the number of dof; the latter is equal to

the number of points employed in the fit minus the number of fitted parameters, i.e.  $\text{dof} = 10 - 1 = 9$ . We then obtain  $\chi_{r,\text{ACT}}^2 = 1.71$  and  $\chi_{r,\text{Planck}}^2 = 2.47$  for ACT and *Planck*, respectively. We notice that the reduced chi-square values suggest a non-optimal goodness of these fits. This can be expected in light of the simplified nature of our theoretical model, which may not capture equally well the gas properties at the void center and at the outer radii. We will come back to this issue in the next section.

Because voids are underdense regions,  $\delta_v$  must satisfy  $-1 \leq \delta_v < 0$ ; we can then infer lower limits on the gas temperature inside voids by saturating  $\delta_v \rightarrow -1$ . By taking into account the uncertainties on our estimates, we find that the mean void electron temperature should satisfy  $T_e > 2.7 \times 10^5 \text{ K}$  for ACT and  $T_e > 5.1 \times 10^5 \text{ K}$  for *Planck* (at 95% C.L.). Results from hydrodynamical simulations (Martizzi et al. 2019) suggest that IGM and WHIM are the major gas phases accounting for the total baryon budget, spanning a broad temperature range from  $10^3 \text{ K}$  to above  $10^6 \text{ K}$ , which accommodates our findings.

We can also use our findings to provide estimates on the ratio between the electron number density in voids  $n_e^v$  and its cosmic mean  $\bar{n}_e$ , assuming uniform density of gas inside voids in Eq. (11), we have:

$$\begin{aligned} \frac{n_e^v}{\bar{n}_e} &= 1 + \delta_v \\ &= 1 - \frac{\delta T \times 10^5 \text{ K}}{T_e} \\ &\leq 1 - \frac{1}{10} \left( -\delta_v \frac{T_e}{10^5 \text{ K}} \right) \\ &\leq \begin{cases} 0.73 & 95\% \text{ C.L. for ACT,} \\ 0.49 & 95\% \text{ C.L. for Planck,} \end{cases} \end{aligned} \quad (16)$$

where the third inequality is taken by assuming the maximum gas temperature in voids to be  $10^6 \text{ K}$  (the denominator in the second equality), as suggested by hydrodynamical simulations (Haider et al. 2016; Martizzi et al. 2019). The fourth inequality is taken by substituting the  $2\sigma$  lower limits from Eq. (15). Therefore, our lower limits in the void electron temperature then translate into upper limits for the void electron density, and where we find again broad agreement between the two data sets.

## 5 CONCLUSIONS

In this paper, we have conducted a stacking analysis of a void catalogue constructed from BOSS galaxy data, over the  $1.6'$  resolution maps of the tSZ Compton  $y$  parameter released by the ACT collaboration, and also the *Planck* MILCA  $y$ -map ( $10'$  resolution) on the same footprint of ACT. We detected the void  $y$ -profile at  $7.3\sigma$  for ACT and  $9.7\sigma$  for *Planck*. Because the void signal we are targeting typically extends over degree angular scales on the sky, the higher resolution of ACT is not a major factor when determining the significance of the detection. Indeed, we observe similar features in both ACT and *Planck* 2D stack maps, and similar trends in their corresponding radial  $y$  profiles, confirming the consistency of our measurements. The uncertainties on the reconstructed profiles were computed by repeating the stacks on a set of 1000 mock catalogues, which also allowed us to evaluate the full covariance matrices associated with the profiles. Finally, we evaluated possible CIB contaminations in our stacks and found that correcting for a CIB leakage provides negligible changes in the profile amplitudes, well below the size of their error bars.

<sup>6</sup> As is shown in Eq. (14), the  $T_e$  and  $\delta_v$  in this model completely degenerate with each other, so it would not be meaningful to fit for the values of each of them separately.

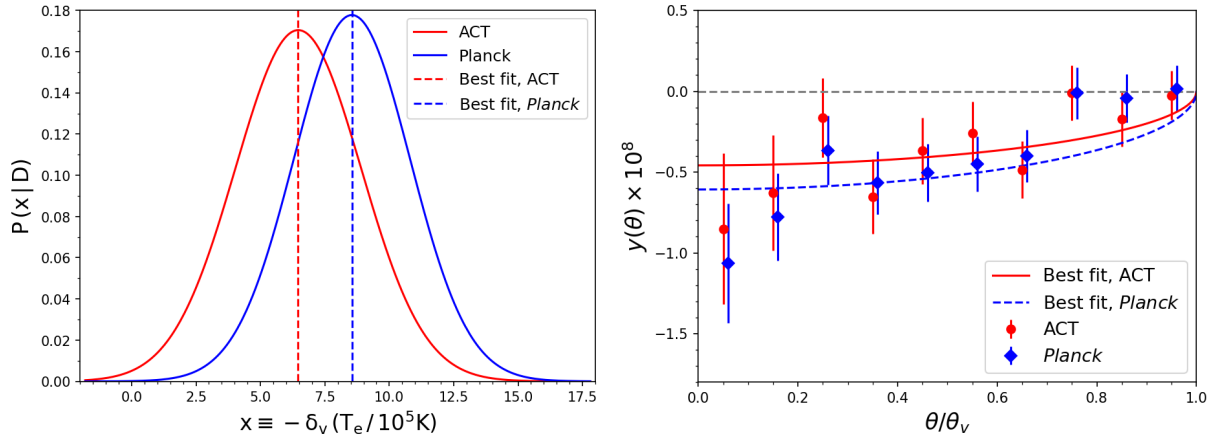


**Figure 7.** *Left*—the posterior probability distribution for the parameter  $(-\delta_v)(T_e/10^5 \text{ K})$  obtained from both ACT (solid red line) and *Planck* (dashed blue line) void stacking data; the vertical lines mark the position of their corresponding best-fit values. *Right*—comparison between the best fit Compton- $y$  profiles (solid red line for ACT, dashed blue line for *Planck*) and the stacked void data, as described in Sec. 4.

We then attempted at reproducing the stacked profiles analytically by using a simple flat-density isothermal model for our voids. Although these are strong assumptions, this is intended to be a preliminary exploration of how the profiles reconstructed from tSZ data can constrain the gas properties within voids. Our model leaves the product between the density contrast and temperature of gas within voids as a free parameter, which we fitted against our measurements to  $-\delta_v \times T_e = (6.5 \pm 2.3) \times 10^5 \text{ K}$  using ACT data and  $-\delta_v \times T_e = (8.6 \pm 2.1) \times 10^5 \text{ K}$  using *Planck* data, with a remarkable agreement between the two data sets. These constraints allowed us to place lower limits on the void gas temperature, at  $2.7 \times 10^5 \text{ K}$  for ACT and  $5.1 \times 10^5 \text{ K}$  for *Planck* (95% C.L.), which fall relatively close to the upper limit of the range spanned by numerical simulation results, suggesting voids may be warmer than expected. An increase in the void gas temperature can be induced by feedback processes from galaxy hosting active galactic nuclei (AGNs), either located inside the void or in its neighbouring region and ejecting hot gas towards the void centre (Constantin et al. 2008; Haider et al. 2016; Martizzi et al. 2019). Our lower limits on  $T_e$  enabled us to assess upper limits on the ratio between the electron number density within voids and its cosmic mean value; the results suggest a deficit of electrons in the void region. Indeed, by setting  $10^6 \text{ K}$  as the highest temperature inside voids, an assumption derived from numerical simulations (Martizzi et al. 2019), the computed fraction of electron number density against the cosmic mean is expected to be below 0.73 (ACT) or 0.49 (*Planck*) at 95% C.L. This results corroborates the finding that voids, as under-dense cosmic structures, are under-pressured relative to the cosmic mean (Alonso et al. 2018). The electron number density in our model is a constant in the voids, which is unrelated with the gas temperature in the voids. We notice that in Bolton et al. (2008), an inverted temperature-density relation is proposed (the middle panel in their Fig. 3), for gas at redshift  $z \approx 2$  with temperature  $T_e < 10^5 \text{ K}$ . But because our work and Bolton et al. (2008) are dealing with gas in different redshifts and temperature regimes, the gas and temperature relation is not always true across different physical conditions. We do notice that one can test this relation once the stacking significance is further improved.

However, we acknowledge that our theoretical model is quite simple and may not be very accurate in capturing the electron density and temperature variations within voids. In fact, the void density may experience significant transitions from its center to its edge (Hamaus

et al. 2014; Chantavat et al. 2017; Verza et al. 2022). Besides, the general linear relation between electron number density and the dark matter density profile may not be accurate in under-dense environments, possibly requiring a position-dependent bias. Finally, the temperature in voids can deviate from the isothermal profile with a complex radial dependence because of the presence of multi-phase gas, as revealed recently by simulations (Haider et al. 2016; Martizzi et al. 2019). Still, because the main goal of our current work is an observational detection of the void signal, we did not explore more detailed models. We leave the implementation of a more accurate theoretical model to a future dedicated study, once the significance of the measurement is further improved.

As a final remark, from an observational perspective, the tSZ signal around voids is generally weak and sensitive to the choice of the void catalogue and the tSZ map. In the future, an optimal reconstruction of high-resolution, large area tSZ signal, with a better cleaning of potential contamination sources, in combination with a larger number of well-selected voids, can undoubtedly improve the results of this type of analysis.

## ACKNOWLEDGEMENTS

We thank useful discussion with David Alonso, Cheng Zhao and Yi-Peng Jing. YZM acknowledges the support of National Research Foundation with Grant No. 150385, and the research program “New Insights into Astrophysics and Cosmology with Theoretical Models Confronting Observational Data” of the National Institute for Theoretical and Computational Sciences of South Africa. DT acknowledges financial support from the XJTLU Research Development Fund (RDF) grant with number RDF-22-02-068. We acknowledge the cosmology simulation database (CSD) in the National Basic Science Data Center (NBSDC) with the funding NBSDC-DB-10.

## DATA AVAILABILITY

The *Planck*  $y$ -map can be downloaded from the *Planck* Legacy Archive website<sup>7</sup>, whereas the ACT  $y$ -map can be downloaded from

<sup>7</sup> <http://pla.esac.esa.int/pla/>



the NASA LAMBDA website<sup>8</sup>. The other data products employed in this work can be delivered for verification purposes under request to the first and corresponding authors.

## REFERENCES

- Alam S., et al., 2017, *MNRAS*, **470**, 2617
- Alonso D., Hill J. C., Hložek R., Spergel D. N., 2018, *Phys. Rev. D*, **97**, 063514
- Aubert M., et al., 2022, *MNRAS*, **513**, 186
- Beygu B., Peletier R. F., van der Hulst J. M., Jarrett T. H., Kreckel K., van de Weygaert R., van Gorkom J. H., Aragon-Calvo M. A., 2017, *MNRAS*, **464**, 666
- Bolton J. S., Viel M., Kim T. S., Haehnelt M. G., Carswell R. F., 2008, *MNRAS*, **386**, 1131
- Bonjean V., Aghanim N., Salomé P., Douspis M., Beelen A., 2018, *A&A*, **609**, A49
- Bregman J. N., 2007, *ARA&A*, **45**, 221
- Cai Y.-C., Padilla N., Li B., 2015, *MNRAS*, **451**, 1036
- Cai Y.-C., Neyrinck M., Mao Q., Peacock J. A., Szapudi I., Berlind A. A., 2017, *MNRAS*, **466**, 3364
- Ceccarelli L., Duplancic F., Garcia Lambas D., 2022, *MNRAS*, **509**, 1805
- Chantavat T., Sawangwit U., Wandelt B. D., 2017, *ApJ*, **836**, 156
- Clampitt J., Jain B., 2015, *MNRAS*, **454**, 3357
- Constantin A., Hoyle F., Vogeley M. S., 2008, *ApJ*, **673**, 715
- Falck B., Koyama K., Zhao G.-B., Cautun M., 2018, *MNRAS*, **475**, 3262
- Fang Y., et al., 2019, *MNRAS*, **490**, 3573
- Fukugita M., Peebles P. J. E., 2004, *ApJ*, **616**, 643
- Górski K. M., Hivon E., Banday A. J., Wandelt B. D., Hansen F. K., Reinecke M., Bartelmann M., 2005, *ApJ*, **622**, 759
- Haider M., Steinhauser D., Vogelsberger M., Genel S., Springel V., Torrey P., Hernquist L., 2016, *MNRAS*, **457**, 3024
- Hamaus N., Sutter P. M., Wandelt B. D., 2014, *Phys. Rev. Lett.*, **112**, 251302
- Hamaus N., Pisani A., Choi J.-A., Lavaux G., Wandelt B. D., Weller J., 2020, *J. Cosmology Astropart. Phys.*, **2020**, 023
- Hartlap J., Simon P., Schneider P., 2007, *A&A*, **464**, 399
- Hill J. C., Spergel D. N., 2014, *J. Cosmology Astropart. Phys.*, **2014**, 030
- Hojjati A., McCarthy I. G., Harnois-Deraps J., Ma Y.-Z., Waerbeke L. V., Hinshaw G., Brun A. M. C. L., 2015, *J. Cosmology Astropart. Phys.*, **2015**, 047
- Hojjati A., et al., 2017, *MNRAS*, **471**, 1565
- Hurier G., Macías-Pérez J. F., Hildebrandt S., 2013, *A&A*, **558**, A118
- Ibitoye A., Tramonte D., Ma Y.-Z., Dai W.-M., 2022, *ApJ*, **935**, 18
- Lavaux G., Wandelt B. D., 2012, *ApJ*, **754**, 109
- Ma Y.-Z., Zhao G.-B., 2014, *Physics Letters B*, **735**, 402
- Ma Y.-Z., Waerbeke L. V., Hinshaw G., Hojjati A., Scott D., Zuntz J., 2015, *J. Cosmology Astropart. Phys.*, **2015**, 046
- Ma Y.-Z., Gong Y., Tröster T., Van Waerbeke L., 2021, *MNRAS*, **500**, 1806
- Macquart J. P., et al., 2020, *Nature*, **581**, 391
- Madhavacheril M. S., et al., 2020, *Phys. Rev. D*, **102**, 023534
- Makiya R., Ando S., Komatsu E., 2018, *MNRAS*, **480**, 3928
- Martizzi D., et al., 2019, *MNRAS*, **486**, 3766
- Melchior P., Sutter P. M., Sheldon E. S., Krause E., Wandelt B. D., 2014, *MNRAS*, **440**, 2922
- Nicastro F., et al., 2018, *Nature*, **558**, 406
- Pandey S., et al., 2022, *Phys. Rev. D*, **105**, 123526
- Pisani A., Sutter P. M., Hamaus N., Alizadeh E., Biswas R., Wandelt B. D., Hirata C. M., 2015, *Phys. Rev. D*, **92**, 083531
- Planck Collaboration et al., 2013, *A&A*, **550**, A134
- Planck Collaboration et al., 2016a, *A&A*, **594**, A22
- Planck Collaboration et al., 2016b, *A&A*, **594**, A23
- Planck Collaboration et al., 2016c, *A&A*, **594**, A27
- Planck Collaboration et al., 2020, *A&A*, **641**, A6
- Pustilnik S. A., Tepliakova A. L., Makarov D. I., 2019, *MNRAS*, **482**, 4329
- Raghunathan S., Nadathur S., Sherwin B. D., Whitehorn N., 2020, *ApJ*, **890**, 168
- Remazeilles M., Delabrouille J., Cardoso J.-F., 2011, *MNRAS*, **410**, 2481
- Sánchez C., et al., 2017, *MNRAS*, **465**, 746
- Shull J. M., Smith B. D., Danforth C. W., 2012, *ApJ*, **759**, 23
- Sunyaev R. A., Zeldovich Y. B., 1970, *Ap&SS*, **7**, 3
- Tanidis K., Camera S., 2021, *arXiv e-prints*, p. arXiv:2107.00026
- Tanimura H., Aghanim N., Douspis M., Beelen A., Bonjean V., 2019, *A&A*, **625**, A67
- Tramonte D., et al., 2023, *ApJS*, **265**, 55
- Verza G., Carbone C., Renzi A., 2022, *ApJ*, **940**, L16
- Vielzeuf P., et al., 2021, *MNRAS*, **500**, 464
- Vikram V., Lidz A., Jain B., 2017, *MNRAS*, **467**, 2315
- Zhao C., Tao C., Liang Y., Kitaura F.-S., Chuang C.-H., 2016, *MNRAS*, **459**, 2670
- de Graaff A., Cai Y.-C., Heymans C., Peacock J. A., 2019, *A&A*, **624**, A48

This paper has been typeset from a  $\text{\TeX}/\text{\LaTeX}$  file prepared by the author.

<sup>8</sup> <https://lambda.gsfc.nasa.gov/product/act/>